Transition Analysis for the CRM-NLF Wind Tunnel Configuration

Pedro Paredes,* Balaji Venkatachari,†
National Institute of Aerospace, Hampton, VA 23666, USA

Meelan M. Choudhari,‡ Fei Li,§ Nathaniel Hildebrand,¶ Chau-Lyan Chang‖
NASA Langley Research Center, Hampton, VA 23681, USA

This paper presents the results of an ongoing study into the linear stability characteristics of the boundary layer flow over the common research model with natural laminar flow (CRM-NLF) aircraft configuration. The flow conditions match selected test conditions from a recent wind tunnel experiment in the National Transonic Facility at the NASA Langley Research Center. Previous work involving parallel stability computations of a boundary layer flow based on the conical flow approximation has shown that the measured onset of laminar-turbulent transition during the experiments can be correlated with the linear amplification of Tollmien-Schlichting (TS) and stationary crossflow (CF) instabilities in the swept wing boundary layer. Here, we examine the effects of the simplifying approximations in both basic state computation and the stability analysis, with the goal of quantifying the resulting changes in the N-factor correlations. Specifically, the basic states are computed by using full Navier-Stokes equations and the stability analysis is performed by using a nonorthogonal coordinate system that allows a clear distinction between planar TS and CF instabilities. Furthermore, the effects of curvature and nonparallel mean flow have been included in the stability computations based on the parabolized stability equations (PSE). The fully turbulent Reynolds-Averaged-Navier-Stokes (RANS) mean flow solutions show good agreement with the measured wall pressure distribution. Viscous-inviscid interactive effects are observed to be important because the shock fronts along the suction surface are influenced by the imposed transition front. The stability results confirm the previous findings related to TS amplification within the inboard region of the wing and the dominance of stationary CF modes in the outboard region. However, given the close proximity of the measured transition front and the dual shock system within the outer part of the wing, the onset of transition may well be shock limited within the outboard region. In general, the transition criterion based on the dual N-factor method with $N_{TS} = N_{CF} = 6$ is reasonably successful at correlating with the measured transition fronts at $Re_{MAC} = 15$ million and $AoA = 1.5,\ 2$ degrees; however, the low values of the correlating N-factors at $Re_{MAC} = 17.5$ million support the hypothesis that the measured transition at the higher Reynolds number may have been strongly influenced by the merging of turbulent wedges that originate from surface imperfections near the leading edge.

Nomenclature

AoA	=	angle of attack [deg]
C_f	=	skin friction coefficient
C_p	=	surface pressure coefficient
f	=	disturbance frequency [Hz]
η_w	=	semispan location nondimensionalized by semispan length

*Research Engineer, Computational AeroSciences Branch, NASA LaRC. AIAA Senior Member
†Research Engineer, Computational AeroSciences Branch, NASA LaRC. AIAA Senior Member
‡Research Scientist, Computational AeroSciences Branch. AIAA Fellow
§Research Scientist, Computational AeroSciences Branch.
¶Research Scientist, Computational AeroSciences Branch. AIAA Member
‖Research Scientist, Computational AeroSciences Branch. AIAA Associate Fellow

h_ξ	=	streamwise metric factor
h_ζ	=	spanwise metric factor
L	=	reference length [m]
M	=	Mach number
N	=	logarithmic amplification factor
$\bar{\mathbf{q}}$	=	vector of base flow variables
$\tilde{\mathbf{q}}$	=	vector of perturbation variables
$\hat{\mathbf{q}}$	=	vector of amplitude variables
Re_{MAC}	=	Reynolds number based on mean aerodynamic chord
Re_∞	=	freestream unit Reynolds number [m^{-1}]
T	=	temperature [K]
(u, v, w)	=	streamwise, wall-normal, and spanwise velocity components [m s^{-1}]
(x, y, z)	=	Cartesian coordinates [m]
x/c	=	chordwise coordinate scaled by reference chord length
y^+	=	near wall grid spacing in wall units
α	=	streamwise wavenumber [m^{-1}]
β	=	spanwise wavenumber [m^{-1}]
λ	=	spanwise wavelength [m]
δ	=	boundary layer thickness [m]
κ_ξ	=	streamwise curvature [m^{-1}]
κ_ζ	=	spanwise curvature [m^{-1}]
ω	=	disturbance angular frequency [rad s^{-1}]
ρ	=	density [kg m^{-3}]
σ	=	spatial growth rate [m^{-1}]
(ξ, η, ζ)	=	streamwise, wall-normal, and spanwise coordinates [m]
Subscript		
∞	=	freestream value
c	=	critical value
Superscript		
H	=	conjugate transpose

I. Introduction

Substantial reductions in the fuel burn of future aircraft have been targeted both in the U.S. [1] and Europe [2] in order to lower the cost of air travel and to alleviate the impact of aviation on the environment. A significant fraction of the targeted reductions in aircraft fuel burn come from reductions in vehicle drag. For today's commercial transport aircraft, up to one half of the total drag corresponds to skin friction drag. Because laminar skin friction is much lower in comparison with the turbulent skin friction, flow control via delayed boundary-layer transition over major aerodynamic surfaces holds the potential to provide the desired reductions in the overall drag.

According to the CFD Vision 2030 [3], the most critical areas in computational fluid dynamics (CFD) simulation capability that will remain a pacing item for the foreseeable future is the ability to adequately predict viscous flows with transition-to-turbulence and flow separation. A majority of CFD computations are carried out under the assumption that the flow is turbulent everywhere, allowing the use of the computationally efficient Reynolds-averaged Navier-Stokes (RANS)-based turbulence models throughout the flowfield. However, for several applications ranging from wings with natural laminar flow (NLF) technology, high-lift configurations, rotorcraft flows, and unmanned aerial vehicles, the strong assumption involving a fully turbulent flow can lead to significant errors in the prediction of relevant performance metrics. Furthermore, most of the RANS models are incapable of modeling the process of transition from laminar to turbulent flow because of the complexity involved in the physics of the transition onset process. The inherent averaging process in the RANS procedure makes it difficult to capture the development of the linear disturbances that initiate the laminar-turbulent transition process within the initially laminar boundary layer as well as the subsequent nonlinear growth of those disturbances and the eventual breakdown to turbulence.

Direct numerical simulations (DNS) and wall-resolved large-eddy simulations (WRLES) are the only approaches capable of simulating the complete set of physical processes that result in the onset of transition and the breakdown of laminar boundary layers into a turbulent flow. However, even with the current state-of-the-art high performance computing tools, these approaches are too expensive to permit the analysis of realistic configurations at high Reynolds numbers due to the extreme requirements on spatio-temporal resolutions. Moreover, DNS and WRLES require accurate specification of the initial and boundary conditions to account for a correct representation of the disturbance environment that excites the instabilities in the flow, and this information is often not fully available from most wind-tunnel and flight tests.

Semiempirical correlations based on linear stability theory (LST), such as the e^N method introduced by Smith and Gamberoni [4] and Ingen [5], remains one of the most widely used approaches for the prediction of transition onset locations in aircraft design computations. The LST equations are derived from the linearized Navier-Stokes equations to track the evolution of small amplitude, fixed frequency disturbances under the parallel flow assumption. The e^N method does require the specification of a critical N-factor that must be obtained from correlations against experimentally measured transition locations. Transition analysis using the parabolized stability equations (PSE) [6] involves less restrictive assumptions and can also account for the effects of a weakly nonparallel basic state, both streamwise and transverse curvatures in the surface geometry, and nonlinear modal interactions of the laminar instabilities. Both LST and PSE can account for the amplification of the dominant primary instabilities encountered on aircraft wings, namely, the Tollmien-Schlichting waves and the stationary and traveling crossflow vortices. However, the application of these approaches toward a coupled computation of laminar, transitional, and fully turbulent parts of a flowfield entails an increased computational cost as well as complexity; it also suffers from a lack of robustness and often requires adequate understanding of transition physics and hydrodynamic stability theory that typical users of CFD codes may not know. To alleviate or circumvent these shortcomings, surrogate models are often used in lieu of the direct computation of stability characteristics based on the laminar flow information provided by the flow solver. There are a number of successful implementations of CFD codes that combine stability-based transition predictions with RANS-based turbulence modeling [7–14]. However, a majority of these models suffer from the need to have sufficiently well-resolved boundary layer profiles in the laminar base-flow computations, including the wall-normal derivatives of velocities and temperature, or at least, the need to compute integral boundary layer parameters that may be used as a proxy to the laminar profiles themselves. These restrictions are difficult to overcome in the modern CFD codes that rely upon massive parallelization and the use of unstructured grids [15].

Given that the vehicle performance is often characterized in terms of integral quantities such as force and moment coefficients or through pressure/skin-friction distribution, capturing the detailed physics of the transition to turbulence in itself is less important than the overall impact of boundary layer transition on the development of the boundary layer and its impact on the aforementioned quantities. Due to the previously mentioned reasons and reduced requirements in terms of computational cost, research efforts to develop models that represent the transition physics and can still be embedded into a RANS framework have gained substantial ground [16–25]. For reasons of computational cost, these models often require that only local information be used to model transition, instead of using detailed boundary layer profiles for stability analysis or even integral-boundary layer parameters that may be used in metamodels for the stability characteristics. The RANS-based transition models often rely on solving additional transport equations and using correlations that determine the onset of transition, allowing the codes to switch between operating in the laminar and turbulent modes. This approach clearly overcomes some of the abovementioned limitations of stability-based transition prediction, and hence, is well-suited for generalizing the established process for turbulent flow computations in a cost effective manner. However, by virtue of lacking an adequate representation of the complex transition process, such models are also less amenable to an extrapolation to new configurations, and in general, must be validated on a case by case basis. More details on the various approaches currently being used to predict/model transition can be found in Refs. [26, 27].

The present research seeks to blend the so-called physics-based approach for transition modeling with the RANS-based approaches, with the eventual goal of developing a reliable and cost efficient, yet robust and user-friendly approach for integrated modeling of laminar-turbulent transition. To help achieve that goal, this particular paper is focused on a detailed assessment of transition prediction via linear stability correlations based on varying levels of fidelity in modeling the amplification of unstable disturbances in the boundary layer flow over a swept, tapered wing. This assessment is facilitated by the transition data obtained on NASA's common research model with natural laminar flow (CRM-NLF) [28–30] that was tested in the National Transonic Facility.

On a typical transport aircraft wing with moderate sweep, transition occurs as a result of crossflow (CF) instability and/or Tollmien-Schlichting (TS) instability, provided that the attachment line remains laminar. The CRM-NLF wing has been designed to modify the surface pressure distribution in such a way that the overall amplification of both of these instabilities is substantially reduced in comparison with that over a conventional wing. CF instability growth is attenuated through a rapid acceleration near the leading edge (achieved via a sufficiently small leading edge radius), while the amplification of the TS waves is controlled by creating a slightly favorable pressure gradient aft of the crossflow dominated leading edge region. The CRM-NLF design also addresses attachment line contamination and the possibility of transition due to attachment line instabilities, thereby allowing the laminar flow to be maintained over substantial regions of the wing, and thus, helping to reduce the total aerodynamic drag.

A bulk of the existing studies involving the transport-equation-based transition models have been carried out for low Mach number ($M_\infty < 0.3$) configurations and/or for modest wing-chord Reynolds numbers and with pressure distributions that may not be optimal for wing designs for subsonic transport aircraft flying at Mach numbers between 0.75 to 0.90. Given the sensitivity of transition to wind tunnel disturbances and the cost of flight experiments, computational tools will need to play an important role in the assessment of laminar flow designs for flight applications, both as a means of risk reduction and to help optimize the wing design. The CRM-NLF configuration supports the simultaneous presence of multiple potential transition mechanisms at realistic flight transport conditions, which makes this configuration a unique opportunity to examine the RANS-based transition models. In that regard, the present paper also aims to provide useful guidance to improve the physical basis of the existing transition models as described in the accompanying paper by Venkatachari et al. [31].

The paper is organized as follows. § II provides a summary of the hierarchy of linear stability formulations used in this paper. The mean flow solutions and instability results for the selected CRM-NLF configuration are presented in §III. Finally, a summary of the present work and some concluding remarks are presented in §IV.

II. Theory

In what follows, we study the boundary layers over the wing of the CRM-NLF at selected conditions from NASA's recent experiments [28–30]. In the conventional approach to study the instability characteristics of wing boundary layers, the local infinite-swept-wing assumption is used to study the evolution of instability waves along the chordwise direction, i.e., perpendicular to the leading edge. Under this assumption, the computational coordinates can be defined as an orthogonal body-fitted coordinate system, with (ξ, η, ζ) denoting the streamwise, wall-normal, and spanwise coordinates and (u, v, w) representing the corresponding velocity components. Density and temperature are denoted by ρ and T. The metric factors are defined as

$$h_\xi = 1 + \kappa_\xi \eta, \quad (1)$$

$$h_\zeta = 1 + \kappa_\zeta \eta, \quad (2)$$

where κ_ξ and κ_ζ denotes the streamwise and spanwise curvatures, respectively. The Cartesian coordinates are represented by (x, y, z). The vector of perturbation fluid variables is $\tilde{\mathbf{q}}(\xi, \eta, \zeta, t) = (\tilde{\rho}, \tilde{u}, \tilde{v}, \tilde{w}, \tilde{T})^T$, the vector of amplitude functions is $\hat{\mathbf{q}}(\eta) = (\hat{\rho}, \hat{u}, \hat{v}, \hat{w}, \hat{T})^T$, and the vector of basic state fluid variables is $\bar{\mathbf{q}}(\eta) = (\bar{\rho}, \bar{u}, \bar{v}, \bar{w}, \bar{T})^T$. The streamwise and spanwise wavenumbers are α and β, respectively, and ω is the angular frequency of the perturbation. The spanwise wavelength is defined as $\lambda = 2\pi/\beta$.

Additionally, the stability characteristics of the three-dimensional boundary layer over the CRM-NLF configurations can also be studied with a nonorthogonal curvilinear coordinate system as implemented in the LASTRAC.3d code [32]. The nonorthogonal curvilinear coordinate system allows the selection of the streamwise direction to be along the surface grid lines that are aligned with the freestream velocity (y-constant lines), while the spanwise direction is selected to be along the spanwise surface grid lines that run parallel to the leading and trailing edges. The remaining coordinate is defined in the wall normal direction. Results for boundary layers over infinite-swept-wing configurations have been shown to be identical between the orthogonal and nonorthogonal coordinate systems [32].

A. Linear Stability Theory

The quasiparallel LST assumes the boundary layer profiles to be locally parallel by dropping the streamwise derivative terms and setting the wall-normal velocity equal to zero. In the LST context, the perturbations have the form

$$\tilde{\mathbf{q}}(\xi, \eta, \zeta, t) = \hat{\mathbf{q}}(\eta) \exp\left[\mathrm{i}\left(\alpha\xi + \beta\zeta - \omega t\right)\right]. \quad (3)$$

Substituting Eq. (3) into the linearized Navier-Stokes (LNS) equations, an ordinary-differential-equation (ODE) based generalized eigenvalue problem (GEVP) can be written in the following form by using the companion matrix method [33] to reduce the quadratic terms in α from the viscous terms,

$$\mathbf{A}\hat{\mathbf{q}}^+ = \alpha \mathbf{B}\hat{\mathbf{q}}^+, \quad (4)$$

where $\hat{\mathbf{q}}^{+}(\eta) = (\hat{\rho}, \hat{u}, \hat{v}, \hat{w}, \hat{T}, \alpha\hat{u}, \alpha\hat{v}, \alpha\hat{w}, \alpha\hat{T})^T$. The entries of operators **A** and **B** are found in Refs. [34, 35]. The GEVP is solved by the inverse Rayleigh iteration method [36]. The imaginary part of the sought eigenvalue α correspond to the growth rate of the disturbance with a selected combination of ω and β.

$$\sigma_{LST}(\xi, \omega, \beta) = -\Im(\alpha) \tag{5}$$

B. Parabolized Stability Equations

In the PSE context, the streamwise curvature and nonparallel effects are considered. The PSE approximation is based on isolating the rapid phase variations in the streamwise direction. The effects of instability wave propagation within a fully three-dimensional boundary layer can also be evaluated by performing the parabolic integration along stream or group velocity lines. The perturbations have the form

$$\tilde{\mathbf{q}}(\xi, \eta, \zeta, t) = \hat{\mathbf{q}}(\xi, \eta) \exp\left[\mathrm{i}\left(\int_{\xi_0}^{\xi} \alpha(\xi')\,\mathrm{d}\xi' + \beta\zeta - \omega t\right)\right], \tag{6}$$

where the unknown, streamwise varying wavenumber $\alpha(\xi)$ is determined in the course of the solution by imposing an additional constraint

$$\int_{\eta} \hat{\mathbf{q}}^H \frac{\partial \hat{\mathbf{q}}}{\partial \xi} h_\xi\, h_\zeta\, \mathrm{d}\eta = 0, \tag{7}$$

which implies a slow variation of the amplitude functions $\hat{\mathbf{q}}(\xi, \eta, \zeta) = (\hat{\rho}, \hat{u}, \hat{v}, \hat{w}, \hat{T})^T$ in the streamwise direction in comparison with the phase term $\exp\left[\mathrm{i}\int_{\xi_0}^{\xi} \alpha(\xi')\,\mathrm{d}\xi'\right]$. Substituting Eq. (6) into the LNS equations and involving the scale separation to neglect the viscous, streamwise derivative terms, one obtains the PSE in the form

$$\left(\mathbf{L} + \mathbf{M}\frac{\partial}{\partial \xi}\right) \hat{\mathbf{q}}(\xi, \eta) = 0. \tag{8}$$

The entries of the coefficient matrices for **L** and **M** with a more detailed description of the method can be found in Refs. [6, 32, 37].

The nonparallel growth rate of the disturbance with a selected combination of ω and β is defined as

$$\sigma_{PSE}(\xi, \omega, \beta) = -\Im(\alpha) + \frac{1}{2}\frac{dK}{d\xi}, \tag{9}$$

and is based on the Kinetic energy norm K calculated with

$$K(\xi) = \int_{\eta} \tilde{\mathbf{q}}(\xi, \eta)^H \mathbf{M}_K \tilde{\mathbf{q}}(\xi, \eta)\, h_\xi\, h_\zeta\, \mathrm{d}\eta, \tag{10}$$

where $\mathbf{M}_K$ is the energy weight matrix,

$$\mathbf{M}_K = \operatorname{diag}\left[0, \bar{\rho}(\xi, \eta), \bar{\rho}(\xi, \eta), \bar{\rho}(\xi, \eta), 0\right]. \tag{11}$$

C. The Dual N-factor Method

The onset of laminar-turbulent transition is estimated using the logarithmic amplification ratio, the so-called N-factor, relative to the lower bound location ξ_{lb} where the disturbance first becomes unstable,

$$N(\omega, \beta) = -\int_{\xi_{lb}}^{\xi} \sigma(\xi', \omega, \beta)\,\mathrm{d}\xi'. \tag{12}$$

Here, we assume that transition onset is likely to occur when a function of N-factor envelope values based on stationary crossflow instability waves, N_{CF}, and based on traveling Tollmien-Schlichting instability waves, N_{TS}, reaches a certain threshold [38, 39]. The expression of the dual $N_{TS} - N_{CF}$ criteria can be written as

$$\left(\frac{N_{TS}}{N_{TS,c}}\right)^{a_{TS}} + \left(\frac{N_{CF}}{N_{CF,c}}\right)^{a_{CF}} = 1, \tag{13}$$

where the subscript c refers to the critical value, and the exponents a_{TS} and a_{CF} control the level of interaction between the two types of instability waves.

III. Results

We begin with a brief overview of the CRM-NLF configuration. Following that, the mean flow solutions at the selected flow conditions are presented. Then, the instability characteristics of those mean flows are analyzed by using the LST as well as the PSE formulations. Finally, the N-factor values determined from the current analysis along the measured transition fronts as reported by Lynde et al. [29] are documented for each of those conditions.

A. Mean Flow Solutions

The CRM is an open geometry representation of a generic transport vehicle and has been used in a multitude of studies [40]. The CRM-NLF builds upon this geometry by replacing the wing with a new one that supports NLF on the upper surface of the wing. The outer mold line (OML) of the CRM-NLF wing was described by using the Constrained Direct Iterative Surface Curvature (CDISC)) NLF design method [41]. The wind-tunnel model is a 5.2% scaled semispan model of the CRM-NLF. The model has a semispan length of 1.5278 m, mean aerodynamic chord of 0.36383 m and a leading-edge sweep of 37.3° outboard of the break, which is reduced to 12.9° over the inboard 10% of the wing. Further details on the CRM-NLF geometry can be found in Ref. [42] and on the CRM webpage (`https://commonresearchmodel.larc.nasa.gov/crm-nlf`).

The experiments were conducted in the National Transonic Facility (NTF) [28–30]. The effective turbulence level of the NTF was estimated by Crouch et al. [43] to be 0.24% based on the variable N-factor correlation proposed by Mack [44] with a critical $N_{TS} = 6$. This turbulence level was confirmed by the direct measurements taken by King et al. [45]. The surface roughness of the model was specified to be 2.28×10^{-5} mm [28].

The mean flow is computed by using NASA's OVERFLOW 2.3b solver [46]. OVERFLOW is a Navier-Stokes solver for structured, overset grids that is capable of computing both time-accurate and steady-state solutions via a variety of options for spatial and temporal discretizations. The CRM-NLF computations are run at three flow conditions that are detailed in Table 1. These flow conditions correspond to problem statement specified by the AIAA Transition Modeling and Prediction workshop organizers (`https://transitionmodeling.larc.nasa.gov/wp-content/uploads/sites/109/2020/02/TransitionMPW_CaseDescriptions.pdf`). This essentially amounts to CFD computations being carried out at a fixed angle of attack instead of fixed lift coefficient that matched the experimentally measured value. Furthermore, these three configurations are selected to study the effect of independent changes of the Reynolds number and the angle of attack. The computations were conducted with adiabatic wall conditions. Solutions with fully turbulent (FT) flow (i.e., without enforcing laminar regions or fixing transition) or transitional flow with imposed transition (IT) front are obtained by using the Spalart-Allmaras (SA) RANS model [47]. In the IT front solutions, the boundary layer remains laminar until the specified location of transition. The mean flow solutions are obtained by running the flow solver in a steady-state manner by using the 3$^{\text{rd}}$-order Roe upwind scheme [48] and the unfactored successive symmetric overrelaxation (SSOR) implicit solution algorithm [49]. The computational grid has six overset near-body blocks (three on the fuselage, one wing-body collar grid, and two on the wing, including its tip). The generation of off-body grids and hole-cutting is performed with the OVERFLOW's domain connectivity function (DCF). The grid has a near-wall spacing of $y^+ \approx 0.5$ and has approximately 40 wall-normal nodes along the boundary layer thickness and 651 nodes around the wing in the chordwise direction, and 401 points in the spanwise direction in the near-body grids. The total number of grid cells is 120 million. Further details of the grid are given by Venkatachari et al. [31].

Table 1 Flow conditions of selected configurations.

Configuration	AoA (°)	Re_{MAC} (10^6)	M_∞	$\bar{T}_{\infty,CFD}$ (K)	$\bar{T}_{\infty,EXP}$ (K)	Re_∞ (10^6 m^{-1})
I	1.44848	14.979	0.85649	241.6538	242.0776	41.101
II	1.44848	17.473	0.85649	241.6538	197.0219	48.039
III	1.98031	14.946	0.85649	241.8234	242.0776	41.028

The approximated transition fronts were extracted from the Temperature Sensitive Paint (TSP) images by Lynde et al. [28, 29]. Figure 1 shows the TSP images for the selected configurations, together with the extracted transition fronts and the approximate location of the shocks from fully turbulent mean flow solutions. The shocks are extracted based on the surface pressure gradients in the computed mean flow solutions. The extracted transition fronts are found to be close to the shocks in the outboard regions of the wing for conditions I and III. Such proximity would indicate that the transition is driven by shock/boundary-layer interactions, instead of by the amplification of CF or TS instability waves. Although

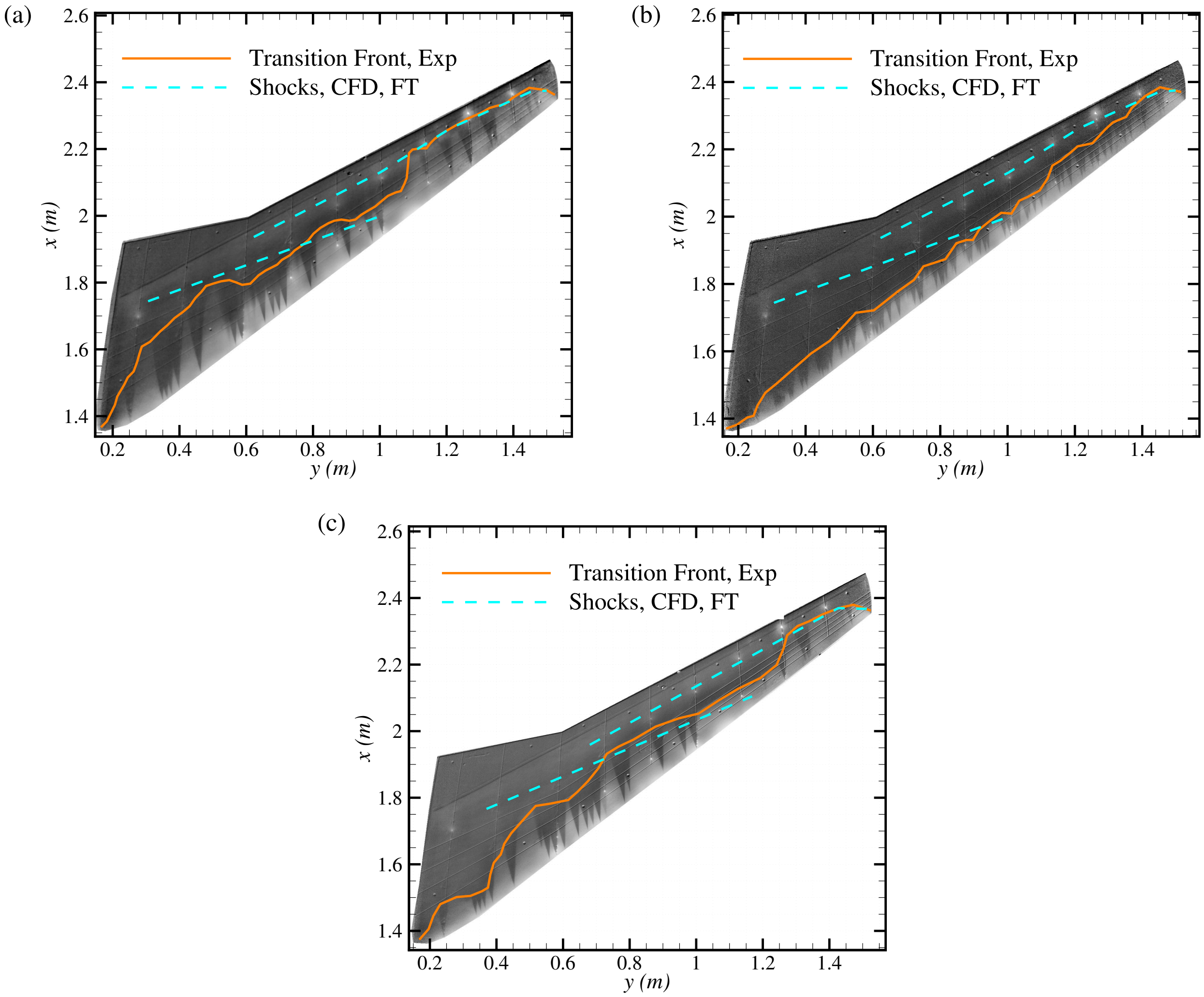

Fig. 1 TSP images with experimental transition front and shock fronts from fully turbulent solutions for configurations (a) I, (b) II, and (c) III.

a large number of turbulent wedges is observed for configuration II (Re_{MAC} = 17.5 × 10^6, AoA = 1.45°), the extracted transition location is located at a more uniform distance from the leading edge and approaches the location of the shocks only in two narrow regions around $y \approx 0.95$ m and close to the tip of the wing. However, the reasons for the drastic upstream shift of the transition front with an increase of 17% of the Reynolds number from configuration I (Fig. 1(a)) to configuration II (Fig. 1(b)) have not yet been fully understood, but surface imperfections are assumed to be the cause for the observed premature transition [29]. The measured transition fronts are used to define the location of the imposed transition fronts used in the transitional mean flow simulations. The imposed transition fronts were defined three to five grid points downstream of the experimentally extracted fronts, and were implemented as discrete piecewise linear segments instead of it being specified at every spanwise grid line (due to constraints within the flow solver).

Figure 2 shows the contours of pressure coefficient over the semispan CRM-NLF model at the selected flow conditions for the transitional simulations with imposed transition fronts. The strong streamwise gradients of the surface pressure coefficient indicate the location of two shocks over the wing for the three configurations. The location of the shocks is visually identical for the two configurations with the same angle of attack and different Reynolds numbers (Figs. 2(a) and 2(b)), but changes for the higher angle of attack case (Fig. 2(c)), with a longer inboard shock that extends from the root to nearly the tip of the wing.

The mean flow solutions for the three configurations detailed in Table 1 are evaluated with the measured surface pressure coefficient, C_p, at the spanwise locations indicated in Fig. 3, where the pressure ports were arranged across

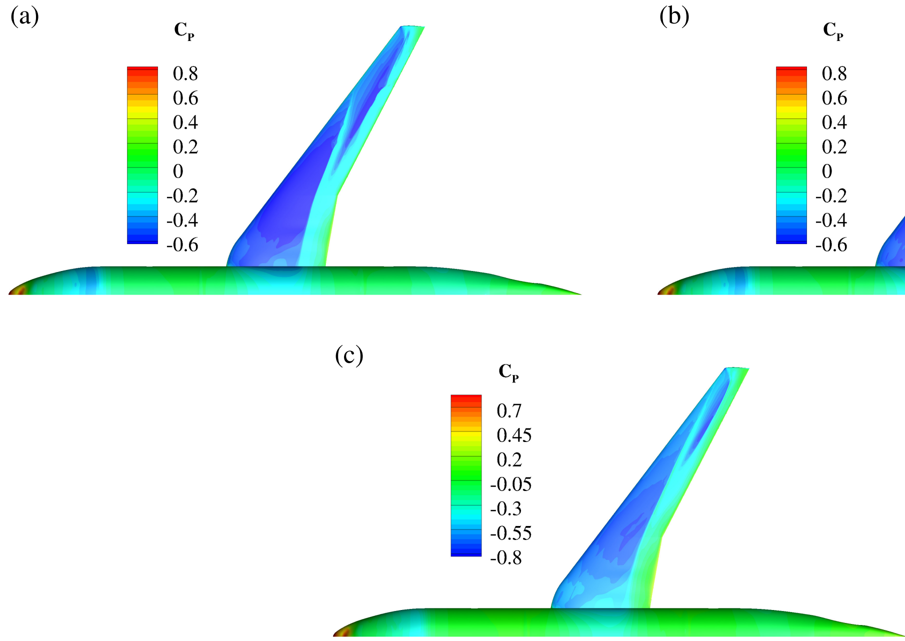

Fig. 2 Surface contours of the pressure coefficient in the imposed transition front solutions of the configurations (a) I, (b) II, and (c) III.

the semispan CRM-NLF model. Figures 4, 5, and 6 show the comparison of the measured and calculated pressure coefficients along rows A through H for the three selected configurations. A reasonable agreement is found between the CFD solutions and experimental measurements across the span of the wing. The suction peak level, the rapid acceleration near the leading edge, and the mild adverse pressure gradient in the midchord section of the upper surface are captured accurately. The pressure levels measured on the suction side of the wing appear to be slightly higher than that predicted by the computations, which was also observed by the computational results shown by Lynde et al. [29]. A significant difference in the location of the shocks is observed between the fully turbulent (FT) and transitional (IT) solutions across the wing span for the three configurations. The shock location is generally well predicted by the fully turbulent computations, but the location is delayed in the transitional solutions, which reflects a high level of viscous-inviscid interaction in the solutions. Furthermore, the pressure ports were deemed to trip the boundary layer and led to early laminar-turbulent transition along the corresponding span locations [28], which would explain the better agreement of the measured values with the fully turbulent simulation results. However, the agreement between the solutions upstream of the shocks is remarkable for both FT and IT solutions.

B. Instability Characteristics

The stability analysis is performed from the attachment line up to the imposed transition front location for the selected span locations. First, we describe the results of stability analysis along selected wing-cut locations for configuration II ($Re_{MAC} = 17.5 \times 10^6$, $AoA = 1.45°$). As previously shown in Fig. 1(b), the transition process is deemed to be less affected by the shocks for this flow condition. The NASA LASTRAC.2d (orthogonal coordinate system) and LASTRAC.3d (nonorthogonal coordinate system) modules of the LASTRAC solver [32, 37] are used to calculate the instability characteristics by using the LST and PSE formulations.

Figure 7 shows the evolution of the N-factor envelope of stationary crossflow (CF) waves with disturbance spanwise wavelengths in the range of $\lambda \in [0.1, 1.4]$ mm along rows A through H. The infinite-swept-wing assumption is invoked for the LST calculations carried out by using the orthogonal coordinate system, and are denoted as 2D in the legend of Fig. 7. Similar results are found with the nonorthogonal LST, denoted as 3D in Fig. 7, although the N-factor values are slightly larger. The PSE calculations are performed with the nonorthogonal coordinate system and includes the effects of nonparallel terms and surface curvature. Nonparallel effects are known to destabilize and curvature effects are known to stabilize the CF instabilities [39]. By adding these terms, the PSE results show a similar trend of the N_{CF} envelopes,

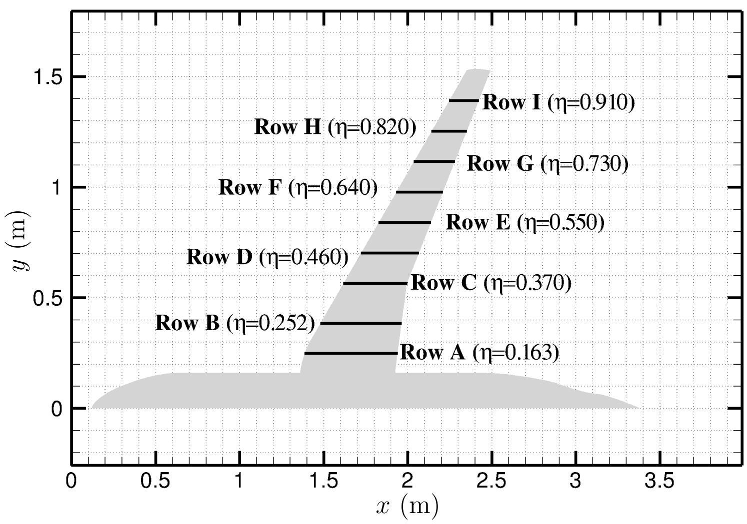

Fig. 3 Spanwise stations where the pressure ports were located in the CRM-NLF model.

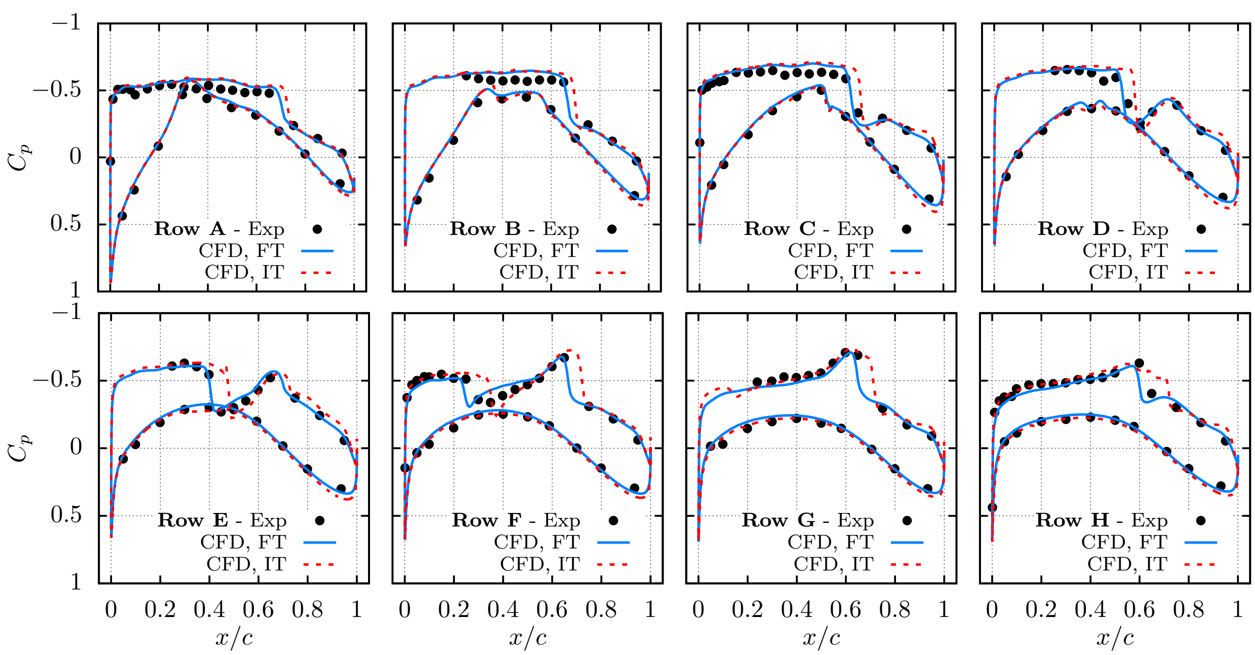

Fig. 4 Experimental and predicted pressure coefficient at selected sections of the wing and configuration I (Re_{MAC} = 15.0 × 10^6, AoA = 1.45°). The solid lines correspond to the fully turbulent (FT) solution and the dashed lines correspond to the imposed transition front (IT) solution.

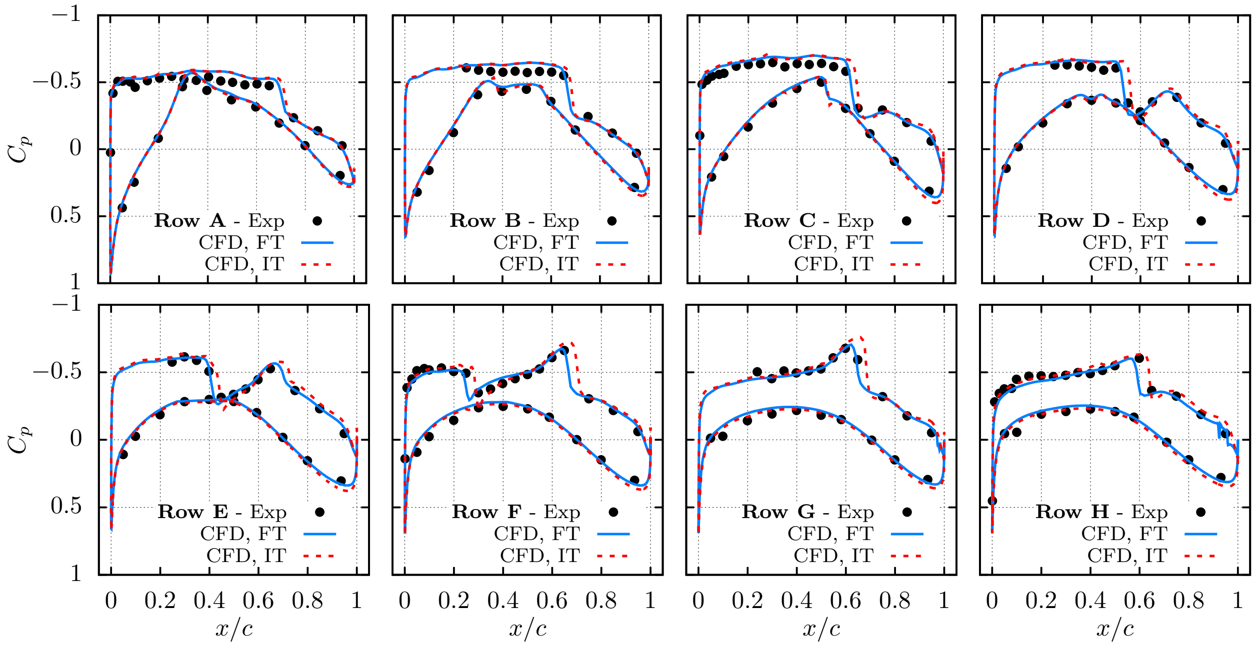

Fig. 5 Experimental and predicted pressure coefficient at selected sections of the wing and configuration II (Re_{MAC} = 17.5 × 10^6, AoA = 1.45°). The solid lines correspond to the fully turbulent (FT) solution and the dashed lines correspond to the imposed transition front (IT) solution.

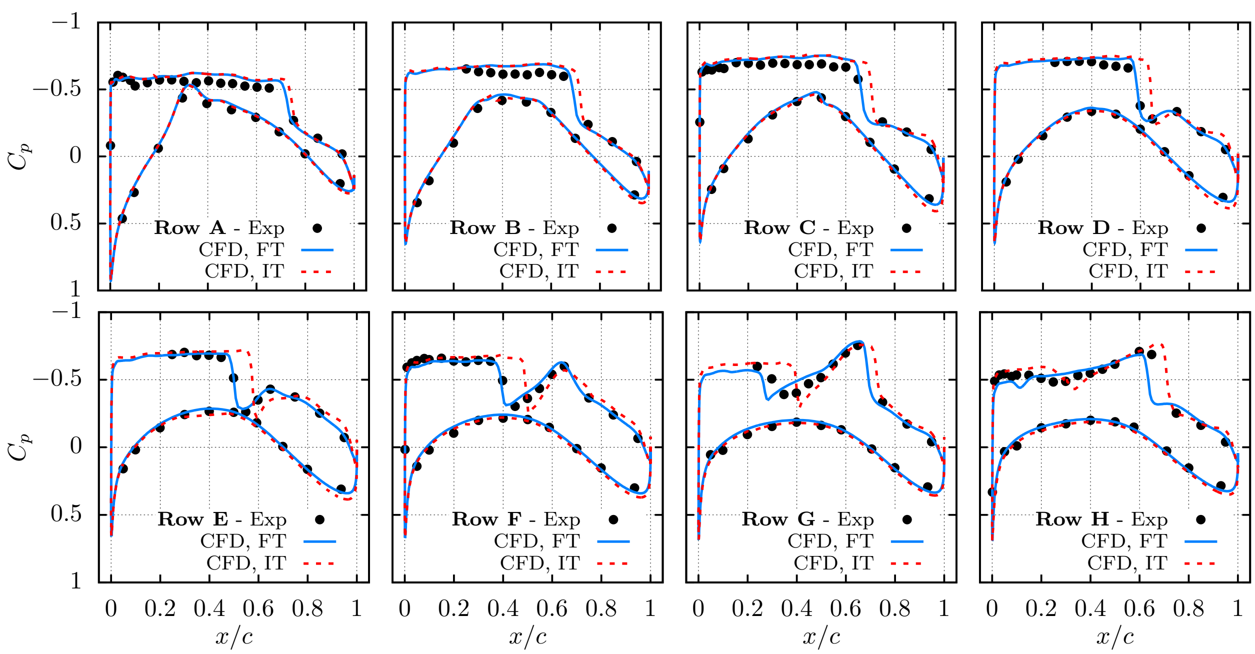

Fig. 6 Experimental and predicted pressure coefficient at selected sections of the wing and configuration III (Re_{MAC} = 15.0 × 10^6, AoA = 1.98°). The solid lines correspond to the fully turbulent (FT) solution and the dashed lines correspond to the imposed transition front (IT) solution.

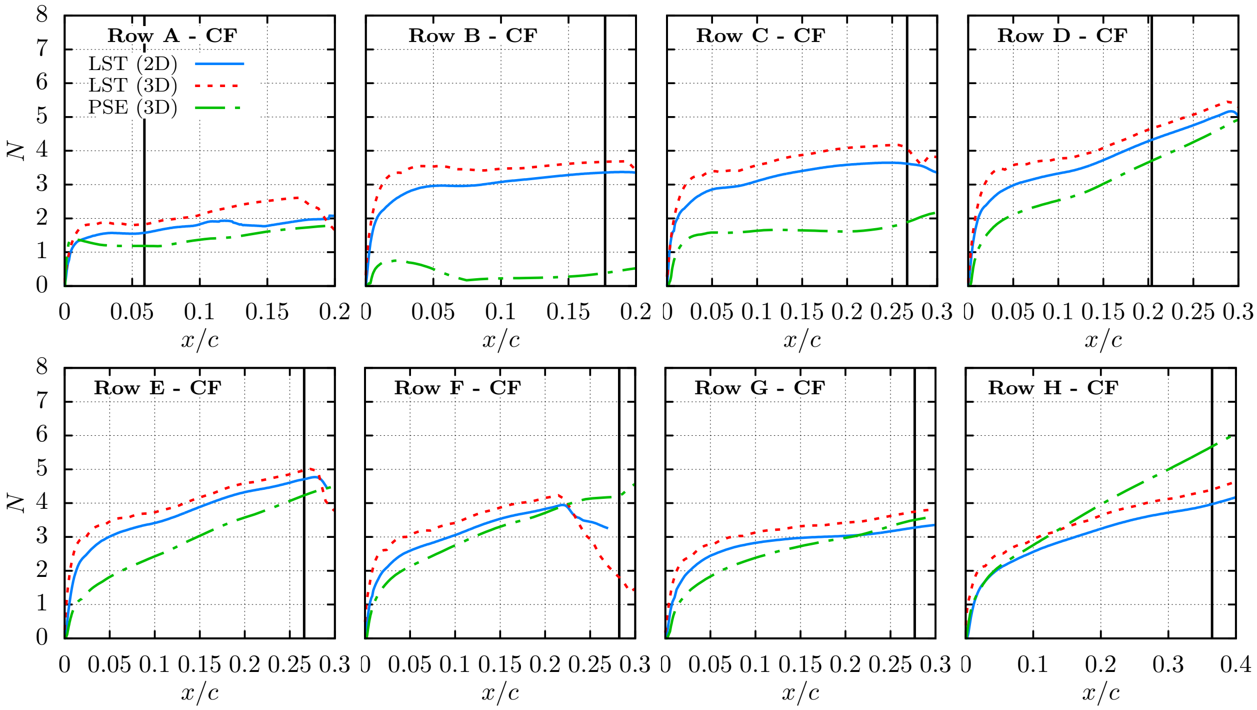

Fig. 7 ***N*-factor calculations based on LST and PSE for stationary crossflow waves with a range of disturbance spanwise wavelengths of $\lambda \in [0.1, 1.4]$ mm for configuration II ($Re_{MAC} = 17.5 \times 10^6$, $AoA = 1.45°$). The vertical, solid, black lines indicate the experimental transition location.**

with slightly lower values than the LST predictions for most of the selected spanwise locations. However, the N-factor values calculated with PSE are found to be substantially smaller for row B and C and larger for row H with respect to the LST predictions. In general, the LST and PSE results show a rapid increase in N_{CF} close to the leading edge and the amplification rate decreases to reach a nearly constant value (rows A, B, C, and G), or continue to grow at a lower rate (rows D, E, F, and H). The N_{CF} value at the transition location computed with PSE (3D) is negligible ($N_{CF} < 2$) for rows A, B, and C, but it is approximately constant ($N_{CF} \approx 4$) for rows D, E, F, and G, and reaches a value of nearly 6 at row H.

Similar results for traveling waves are shown in Fig. 8. For three-dimensional boundary layers, a clear distinction between TS and traveling CF waves is often not possible when the conventional infinite-swept-wing approach is used with an orthogonal coordinate system, because only a single unstable mode is found for some regions of the parameter space of disturbance spanwise wavenumber and frequency. However, the use of a nonorthogonal curvilinear coordinate system with streamwise direction aligned with the flow direction allows a more consistent definition of traveling CF (large spanwise wavenumbers, $\beta \neq 0$) and planar TS (zero spanwise wavenumber, $\beta = 0$) instability waves. The streamlines are approximately aligned with the freestream flow direction downstream of the leading-edge region. Therefore, instability waves with $\beta = 0$ correspond to planar waves with respect to the approximate streamline direction and can be identified as TS waves. Furthermore, planar waves are known to be the most unstable TS waves at subsonic conditions. However, in the infinite-swept-wing approach with an orthogonal coordinate system, $\beta = 0$ implies wave angles perpendicular to the leading edge, or equivalently, a wave angle with respect to the boundary-layer edge that is approximately equal to the local sweep wing angle. Because of this, the orthogonal LST (2D) results shown in Fig. 8 are computed with small spanwise wavenumbers, i.e., $|\beta| \leq 1.2566 \times 10^3$ m^{-1}, to include traveling waves with wave angles in the direction of the streamlines. For the three approaches, the disturbance frequencies are selected in the range of $f \in [10, 120]$ kHz. The comparison of N-factor envelopes computed with orthogonal LST and nonorthogonal LST and PSE of Fig. 8 shows similar results for the three approaches. The orthogonal LST N-factor values are slightly larger than the nonorthogonal LST values due to the addition of the oblique traveling crossflow waves. The nonorthogonal PSE results are slightly lower than those for the nonorthogonal LST due to the addition of the nonparallel effects. The effects of curvature and nonparallel terms are less remarkable for the TS than for the CF waves (Fig. 7), because those

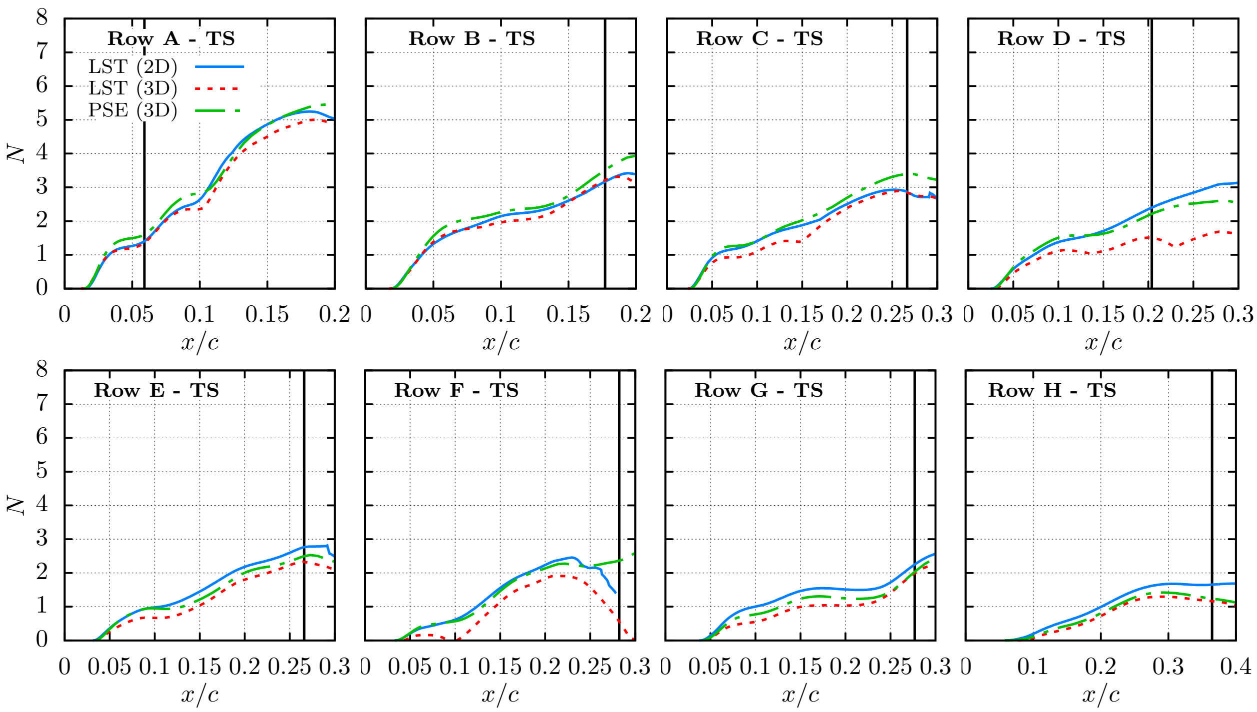

Fig. 8 **N-factor calculations based on LST and PSE for traveling waves with a range of disturbance frequencies of $f \in [10, 120]$ kHz and spanwise wavenumber of $\beta = 0$ for the nonorthogonal (3D) LST and PSE results, while the spanwise wavenumber is selected equal to $\beta = -1.2566 \times 10^3$, -6.2832×10^4, 0, 6.2832×10^4, and 1.2566×10^3 m^{-1} for the orthogonal (2D) LST results. The flow conditions correspond to configuration II ($Re_{MAC} = 17.5 \times 10^6$, $AoA = 1.45°$). The vertical, solid, black lines indicate the experimental transition location.**

are mostly important in the immediate vicinity of the attachment line, where the TS waves are stable. The maximum N_{TS} values are found to decrease as the wing span location increases from row A to row H.

Next, the N-factor envelope results computed with the nonorthogonal PSE are discussed for each of the three configurations detailed in Table 1. Figures 9(a) and 9(b) shows the contours of N_{CF} and N_{TS}, respectively, within the laminar region of the solution for configuration I ($Re_{MAC} = 15.0 \times 10^6$, $AoA = 1.45°$). High N_{CF} values larger than 6 are found in a narrow region just inboard of the break, as well as in the midspan region of the wing from $y = 0.65$ mm to 0.85 m, and in the outboard region of the wing for $y > 1.1$ m. However, as the imposed transition front is located close to the shocks, the flow appears to separate at some of these locations. The N_{TS} contours of Fig. 9(b) show a good agreement of the $N_{TS} \approx 7$ with the experimental transition front in the inboard region of the wing within the range of $y \in [0.3, 0.55]$ m. The value of N_{TS} decreases at farther outboard stations (i.e., larger values of y), where the transition front is approximately aligned with the second (i.e., aft) shock. A local peak of N_{TS} is found at $y = 1.1$ m that is associated with a laminar separation bubble induced by the inboard shock. The results of Fig. 10 for configuration II ($Re_{MAC} = 17.5 \times 10^6$, $AoA = 1.45°$) are limited to the shorter laminar flow acreage across most of the wing span. The N_{CF} values are found to be moderate, i.e., $N_{CF} \approx 4$ over a long region within the middle of the wing span, but increases significantly in the outboard region of the wing. For this case, the measured transition in the outboard region does not fully overlap with the shock as seen for configuration I in Fig. 9. In this region, i.e., $y \in (1.15, 1.35)$ m, the N_{CF} values are significantly larger and the $N_{CF} = 6$ isoline roughly aligns with the experimental transition front. The N_{TS} results shown in Fig. 10(b) show moderate N_{TS} values between 3 and 4 along the experimental transition front up to the break, i.e., for $y < 0.6$ m. The N_{TS} is lower than 3 outboard of the break with the exception of a local peak near $y = 1.05$ m that is attributed to a laminar separation bubble induced by the shock. The effect of the angle of attack is studied in Fig. 11, which shows the N_{CF} and N_{TS} results for configuration III ($Re_{MAC} = 15.0 \times 10^6$, $AoA = 1.98°$). In this case, the N_{CF} values are significant, i.e., $N_{CF} > 5$, in a narrow region located in the inboard vicinity of the break, similar to Fig. 9(a) for configuration I, and in the outermost region, although the transition front coincides with the shock front. On the other hand, the N_{TS} values along the measured transition front are appreciably large ($N_{TS} > 5$) up

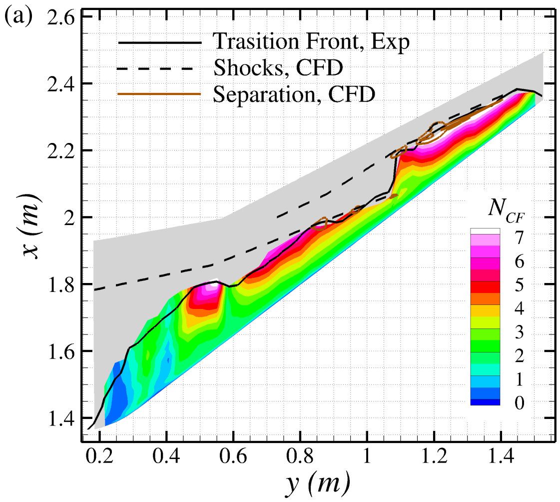

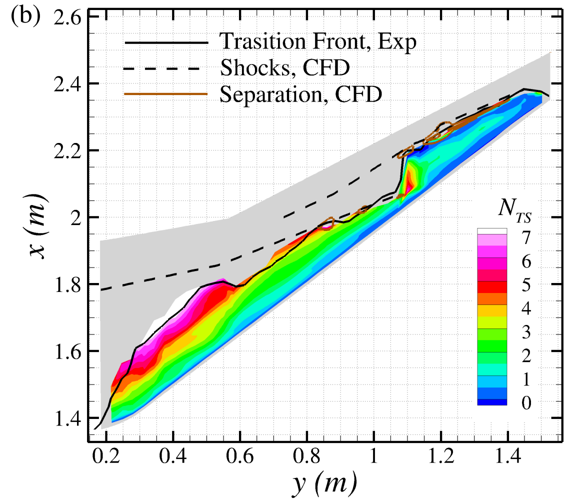

Fig. 9 ***N*-factor contours of (a) stationary CF waves ($f = 0$) and (b) TS waves ($\beta = 0$) calculated with nonorthogonal PSE for configuration I ($Re_{MAC} = 15.0 \times 10^6$, $AoA = 1.45°$).**

to $y = 0.9$ m. For $y > 0.9$ m, the experimental transition front is located close to the shocks.

The dual $N_{TS} - N_{CF}$ criterion of Eq. (13) is evaluated by using the present nonorthogonal PSE results in Fig. 12. The pairs of N_{CF} and N_{TS} values are plotted for each spanwise grid location along the experimental transition front, except for the portions that appear to be influenced by flow separation. A large scatter in the N_{TS} and N_{CF} pairs is observed. As previously observed in the N-factor contours in Figs. 9, 10, and 11, the N_{TS} values reached for configuration II are lower than those for the other two configurations due to the significantly shorter laminar acreage across the wing span. The $N_{CF} - N_{TS}$ curves plotted in Fig. 12 use $N_{CF,c} = 6$, $a_{TS} = 3$, and $a_{CF} = 3$, while $N_{TS,c} = 6$ is used for the solid line and $N_{TS,c} = 3.2$ is used for the dashed line. The $N_{TS,c} = 6$ is the value used by Crouch et al. [43] to correlate measured transition locations on a wing body configuration tested in the same facility. Although the results for configuration II seem to cluster around the dashed line, such a large decrease in $N_{TS,c}$ is not expected for this small variation in the Reynolds number with respect to the Reynolds number of the other configurations. The large number of wedges observed in the TSP image for configuration II (Fig. 1(b), $Re_{MAC} = 17.5 \times 10^6$, $AoA = 1.45°$) was deemed to indicate early transition due to particulate contamination [29]. On the other hand, the results for configurations I and III ($Re_{MAC} = 15.0 \times 10^6$) show large scatter around the solid line with $N_{TS,c} = 6$. The predicted transition locations where the critical $N_{TS}(N_{CF})$ value defined by Eq. (13) with $N_{TS,c} = N_{CF,c} = 6$, and $a_{TS} = a_{CF} = 3$ are shown in Figs. 13(a) and 13(c) for configurations I and III. Figure 13(b) shows the predicted transition locations for configuration II with the same constants but the lower critical N_{TS} value of $N_{TS,c} = 3.2$. Note that predicted transition locations are available only at the span locations where the data reach the critical value within the laminar region of the solution. In general, the predicted transition locations show an acceptable agreement with the experimental transition fronts.

IV. Summary and Concluding Remarks

Linear stability analysis of the three-dimensional boundary layer flow over the CRM-NLF aircraft configuration is presented. Flow conditions are selected to match those from a recent wind tunnel experiment in the National Transonic Facility at the NASA Langley Research Center [28–30]. Three configurations are selected to study the effect of the Reynolds number and of the angle of attack, namely, $(Re_{MAC}, AoA)_I = (15.0 \times 10^6, 1.45°)$, $(Re_{MAC}, AoA)_{II} = (17.5 \times 10^6, 1.45°)$, and $(Re_{MAC}, AoA)_{III} = (15.0 \times 10^6, 1.98°)$. The mean flow solutions are calculated with the OVERFLOW 2.3b solver as having fully turbulent flow or also as partly laminar flow with an imposed transition front on the upper surface of the wing along with the Spalart-Allmaras turbulence model in the fully turbulent portion of the flow. The pressure coefficients are found to agree well with the measured values at selected wingspan stations, although the imposed transition front solutions show a consistent downstream shift of the shock location with respect to the fully turbulent solutions and with respect to the experimental measurements. This shift indicates that the solution is sensitive to the effects of viscous-inviscid interaction, although the agreement along the

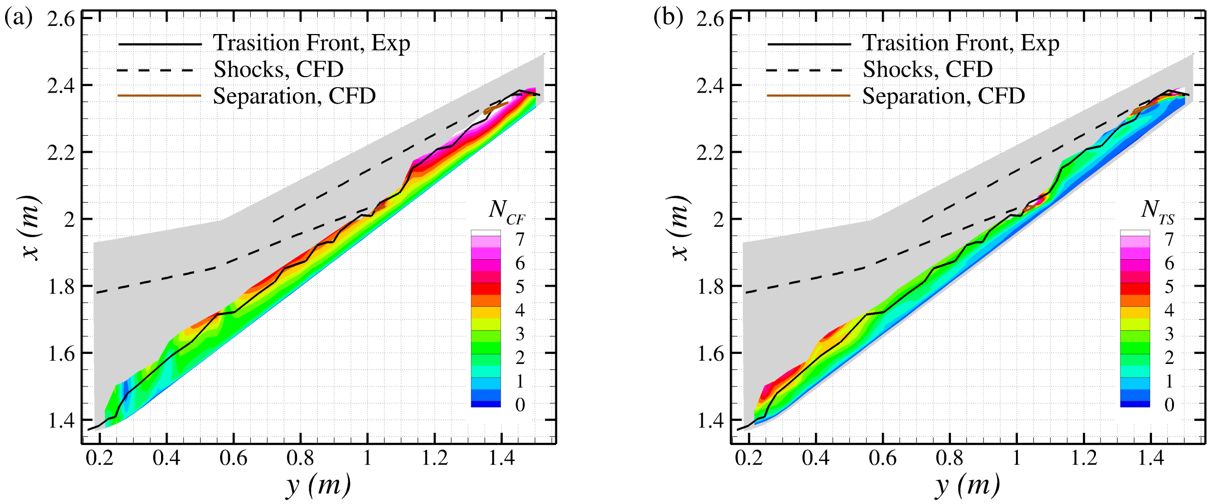

Fig. 10 ***N*-factor contours of (a) stationary CF waves ($f = 0$) and (b) TS waves ($\beta = 0$) calculated with nonorthogonal PSE for configuration II ($Re_{MAC} = 17.5 \times 10^6$, $AoA = 1.45°$).**

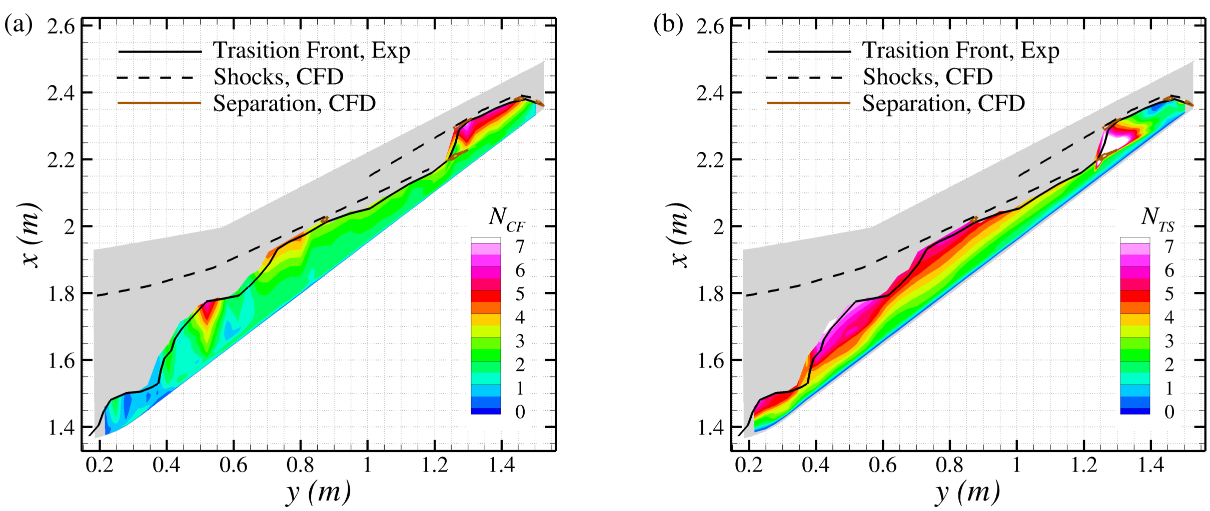

Fig. 11 ***N*-factor contours of (a) stationary CF waves ($f = 0$) and (b) TS waves ($\beta = 0$) calculated with nonorthogonal PSE for configuration III ($Re_{MAC} = 15.0 \times 10^6$, $AoA = 1.98°$).**

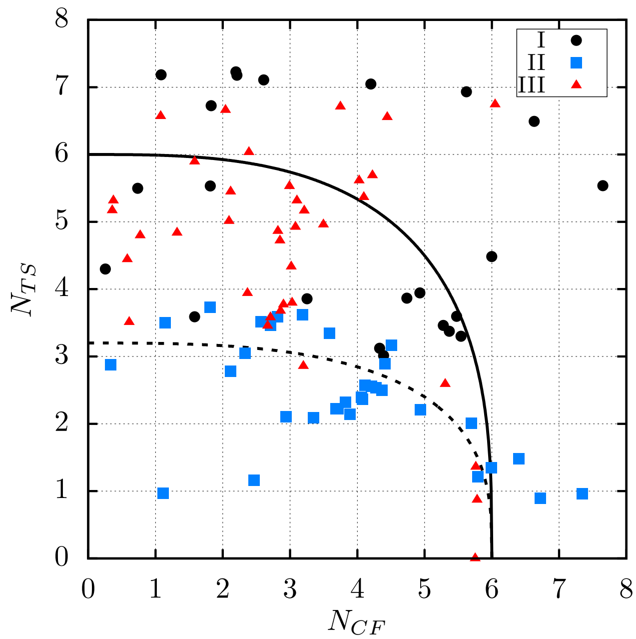

Fig. 12 N-factors values at experimental transition locations for stationary CF waves (N_{CF}) and TS waves (N_{TS}) calculated with nonorthogonal PSE for selected configurations.

laminar region of the solution is not visually altered. During the experiments, the pressure ports were likely tripping the boundary layer and inducing an early transition along those spanwise stations [29] and that would explain the better agreement of the fully turbulent solution at those stations.

The stability results extend the previously reported findings by Lynde et al. [28, 29] by considering basic states that are computed by using full Navier-Stokes equations instead of boundary-layer equations together with the conical flow approximation, as well as a more general formulation of the stability analysis by using a nonorthogonal coordinate system that allows for the distinction of stationary crossflow (CF) waves (nonzero spanwise wavenumber) and planar Tollmien-Schlichting (TS waves) (nonzero frequency and zero spanwise wavenumber). Furthermore, the effects of surface curvature and a nonparallel mean flow, which are particularly important in the immediate vicinity of the wing leading edge, are included in the stability computations based on the parabolized stability equations (PSE). The logarithmic amplification factors of CF (N_{CF}) and TS (N_{TS}) instability waves are calculated across the wing span of each selected configuration.

While the present study is still ongoing, the results obtained so far indicate that the transition front in the region inboard of the Yehudi break (except in the vicinity of the break line) is dominated by TS amplification for the configurations I and III with $Re_{MAC} = 15.0 \times 10^6$. On the other hand, appreciably large values of N_{CF} are found within the outboard region. However, the front is approximately aligned with the shock front, and also indicates a rapid jump from the upstream shock to the downstream shock near the spanwise station where the inboard shock appears to terminate. For the larger angle of attack of 1.98°, the crossflow instability becomes significantly weaker over most of the wing span, with relatively larger N_{CF} observed only near the wing tip, although the transition front again coincides with the outboard shock. Given these observations, the transition front is deemed to be shock limited at these spanwise stations. The low N-factor values at ($Re_{MAC} = 17.5 \times 10^6$ confirm a premature onset of transition at that condition, presumably as a result of the merging of the large number of transition wedges revealed by the TSP image [29]. However, the transition within the outboard region is again dominated by stationary CF amplification.

Finally, the dual $N_{TS} - N_{CF}$ criterion [39] is evaluated by using the present results together with the experimental transition front. The critical N_{CF} is set to 6 and the critical N_{TS} is set to 6, following the study of Crouch et al. [43], which correlated the measured transition locations on a wing body configuration tested in the same facility. A lower N_{TS} is used to correlate the $Re_{MAC} = 17.5 \times 10^6$ case because of the early transition observed for this case. Despite the large scatter observed in the $N_{TS} - N_{CF}$ pairs, the predicted transition locations at several spanwise locations where the stability data reach the critical $N_{TS}(N_{CF})$ value show a favorable agreement with the experimental transition location. Transition analysis for the lower Reynolds number configurations and for additional angles of attack will be part of the

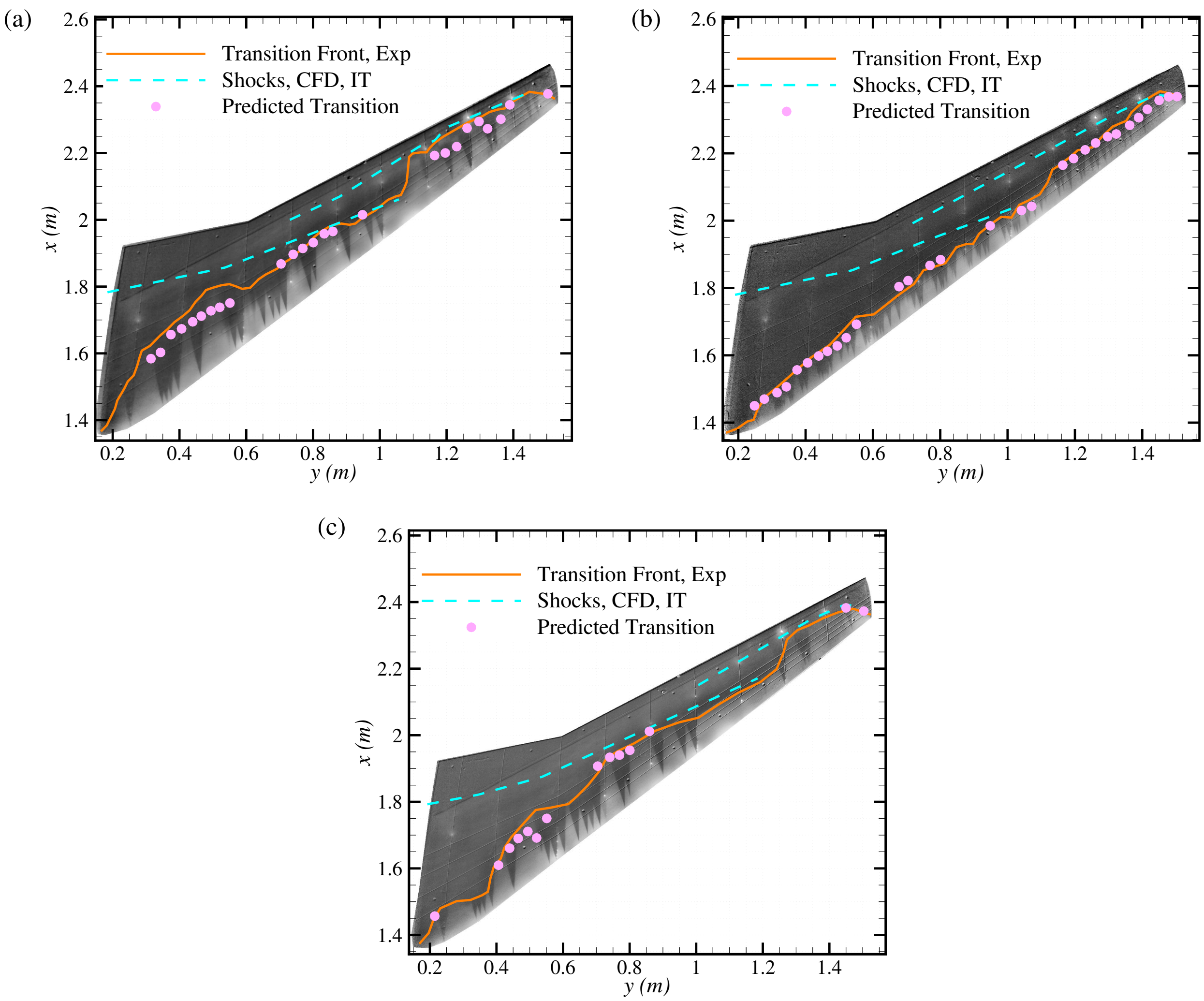

Fig. 13 Predicted transition locations using the dual $N_{TS} - N_{CF}$ criteria at available span locations over the TSP images shown along with experimental transition front and shock fronts from imposed transition front solutions for configurations (a) I ($N_{TS,c} = 6$), (b) II ($N_{TS,c} = 3.2$), and (c) III ($N_{TS,c} = 6$).

follow-on work.

Given the computations reported herein were carried out under the conditions of fixed angle of attack, it will be of useful to make comparisons against experimental data by performing the CFD computations under the assumption of fixed lift coefficient. The results from those computations will also be reported in a future work.

Acknowledgments

This research is sponsored by the NASA Transformational Tools and Technologies (TTT) project of the Transformative Aeronautics Concepts Program under the Aeronautics Research Mission Directorate. The first two authors' research is funded through the National Institute of Aerospace (NIA) under the cooperative agreement 2A00 (Activity 201133). The computational resources supporting this work were provided by the K midrange cluster at NASA Langley Research Center and by the NASA High-End Computing (HEC) Program through the NASA Advanced Supercomputing (NAS) Division at the Ames Research Center. The authors would like to acknowledge Richard Campbell, Michelle Lynde, and Sally Viken for sharing details about the CRM-NLF experiment and associated computations.

References

[1] *Subsonic Fixed Wing Project Overview*, NASA FAP 2008 Annual Meeting, Atlanta, 2008.

[2] Report of the Group of Personalities, "European Aeronautics: A Vision for 2020," Europan Commission Rept. KI-34-01-827-EN-C, January 2001.

[3] Slotnick, J., Khodadoust, A., Alonso, J., Darmofal, D., Gropp, W., Lurie, E., and Mavriplis, D., "CFD Vision 2030 Study: A Path to Revolutionary Computational Aerosciences," Tech. Rep. CR-2014-218178, NASA, 2014.

[4] Smith, A. M. O., and Gamberoni, N., "Transition, Pressure Gradient and Stability Theory," Tech. Rep. ES-26388, Douglas Aircraft Division, 1956.

[5] Ingen, J. L. v., "A Suggested Semi-Empirical Method for the Calculation of the Boundary Layer Transition Region," *Technische Hogeschool Delft, Vliegtuigbouwkunde, Rapport VTH-74*, 1956.

[6] Herbert, T., "Parabolized Stability Equations," *Annual Review of Fluid Mechanics*, Vol. 29, No. 1, 1997, pp. 245–283. doi:10.1146/annurev.fluid.29.1.245.

[7] Campbell, R., Campbell, M., and Streit, T., "Progress Toward Efficient Laminar Flow Analysis and Design," AIAA Paper 2011-3527, 2011. doi:10.2514/6.2011-3527.

[8] Cliquet, J., Houdeville, R., and Arnal, D., "Application of Laminar-Turbulent Transition Criteria in Navier-Stokes Computations," *AIAA Journal*, Vol. 46, No. 5, 2008, pp. 1182–1190. doi:10.2514/1.30215.

[9] Davis, M. B., Reed, H., Youngren, H., Smith, B., and Bender, E., "Transition Prediction Method Review Summary for the Rapid Assessment Tool for Transition Prediction (RATTraP)," Tech. Rep. AFRL-VA-WP-TR-2005-3130, Lockheed Martin Corporation, June 2005.

[10] Drela, M., "Implicit Implementation of the Full En̂ Transition Criterion," AIAA Paper 2003-4066, Jun 2003. doi:10.2514/6.2003-4066.

[11] Drela, M., and Giles, M. B., "Viscous-Inviscid Analysis of Transonic and Low Reynolds Number Airfoils," *AIAA Journal*, Vol. 25, No. 10, 1987, pp. 1347–1355. doi:10.2514/3.9789.

[12] Krumbein, A., Krimmelbein, N., and Grabe, C., "Streamline-Based Transition Prediction Techniques in an Unstructured Computational Fluid Dynamics Code," *AIAA Journal*, Vol. 55, No. 5, 2017, pp. 1548–1564. doi:10.2514/1.J054990.

[13] Krumbein, A. M., "Automatic Transition Prediction and Application to Three-Dimensional Wing Configurations," *Journal of Aircraft*, Vol. 44, No. 1, 2007, pp. 119–133. doi:10.2514/1.22254.

[14] Perraud, J., Arnal, D., Casalis, G., Archambaud, J.-P., and Donelli, R., "Automatic Transition Predictions using Simplified Methods," *AIAA Journal*, Vol. 47, No. 11, 2009, pp. 2676–2684. doi:10.2514/1.42990.

[15] Stock, H. W., and Haase, W., "Navier-Stokes Airfoil Computations with E Transition Prediction Including Transitional Flow Regions," *AIAA Journal*, Vol. 38, No. 11, 2000, pp. 2059–2066. doi:10.2514/2.893.

[16] Warren, E. S., and Hassan, H. A., "Transition Closure Model for Predicting Transition Onset," *Journal of Aircraft*, Vol. 35, No. 5, 1998, pp. 769–775. doi:10.2514/2.2368.

[17] Edwards, J. R., Roy, C. J., Blottner, F. G., and Hassan, H. A., "Development of a One-Equation Transition/Turbulence Model," *AIAA Journal*, Vol. 39, No. 9, 2001, pp. 1691–1698. doi:10.2514/2.1526.

[18] Walters, D. K., and Leylek, J. H., "A New Model for Boundary Layer Transition using a Single-Point RANS Approach," *Journal of Turbomachinery*, Vol. 126, No. 1, 2004, pp. 193–202.

[19] Menter, F. R., Langtry, R., and Völker, S., "Transition Modelling for General Purpose CFD Codes," *Flow, Turbulence and Combustion*, Vol. 77, No. 1, 2006, pp. 277–303. doi:10.1007/s10494-006-9047-1.

[20] Langtry, R. B., and Menter, F. R., "Correlation-Based Transition Modeling for Unstructured Parallelized Computational Fluid Dynamics Codes," *AIAA Journal*, Vol. 47, No. 12, 2009, pp. 2894–2906. doi:10.2514/1.42362.

[21] Medida, S., and Baeder, J., "Application of the Correlation-Based $\gamma - Re_{\theta}t$ Transition Model to the Spalart-Allmaras Turbulence Model," AIAA Paper 2011-3979, 2011. doi:10.2514/6.2011-3979.

[22] Wang, S., Liang with Fu, "RANS Modeling of High-Speed Aerodynamic Flow Transition with Consideration of Stability Theory," *Progress in Aerospace Sciences*, Vol. 58, 2013, pp. 36–59. doi:10.1016/j.paerosci.2012.08.004.

[23] Ge, X., Arolla, S., and Durbin, P., "A Bypass Transition Model Based on the Intermittency Function," *Flow, Turbulence and Combustion*, Vol. 93, No. 1, 2014, pp. 37–61.

[24] Coder, J. G., and Maughmer, M. D., "Computational Fluid Dynamics Compatible Transition Modeling using an Amplification Factor Transport Equation," *AIAA Journal*, Vol. 52, No. 11, 2014, pp. 2506–2512. doi:10.2514/1.J052905.

[25] Coder, J. G., "Further Development of the Amplification Factor Transport Transition Model for Aerodynamic Flows," AIAA Paper 2019-0039, Jan 2019. doi:10.2514/6.2019-0039.

[26] Medida, S., "Correlation-Based Transition Modeling for External Aerodynamic Flows," Ph.D. thesis, University of Maryland, 2014.

[27] Krumbein, A., Krimmelbein, N., Grabe, C., and Shengyang, N., "Development and Application of Transition Prediction Techniques in an Unstructured CFD Code (Invited)," AIAA Paper 2015-2476, 2015. doi:10.2514/6.2015-2476.

[28] Lynde, M. N., Campbell, R. L., Rivers, M. B., Viken, S. A., Chan, D. T., Watkins, A. N., and Goodliff, S. L., "Preliminary Results from an Experimental Assessment of a Natural Laminar Flow Design Method," AIAA Paper 2019-2298, 2019. doi:10.2514/6.2019-2298.

[29] Lynde, M. N., Campbell, R. L., and Viken, S. A., "Additional Findings from the Common Research Model Natural Laminar Flow Wind Tunnel Test," AIAA Paper 2019-3292, 2019. doi:10.2514/6.2019-3292.

[30] Rivers, M. B., Lynde, M. N., Campbell, R. L., Viken, S. A., Chan, D. T., Watkins, A. N., and Goodliff, S. L., "Experimental Investigation of the NASA Common Research Model with a Natural Laminar Flow Wing in the NASA Langley National Transonic Facility," AIAA Paper 2019–2189, 2019. doi:10.2514/6.2019-2189.

[31] Venkatachari, B., Paredes, P., Derlaga, J., Buning, P., Chouhdari, M., Li, F., and Chang, C.-L., "Assessment and Improvement of RANS-Based Transition Models Based on Experimental Data of the Common Research Model with Natural Laminar Flow," AIAA 2021-0000, 2021.

[32] Chang, C.-L., "LASTRAC.3d: Transition Prediction in 3D Boundary Layers," AIAA Paper 2004-2542, 2004.

[33] Bridges, T. J., and Morris, P. J., "Differential Eigenvalue Problems in Which the Parameter Appears Nonlinearly," *Journal of Computational Physics*, Vol. 55, No. 3, 1984, pp. 437–460.

[34] Malik, M. R., "Numerical Methods for Hypersonic Boundary Layer Stability," *Journal of Computational Physics*, Vol. 86, 1991, pp. 376–413.

[35] Paredes, P., "Advances in Global Instability Computations: from Incompressible to Hypersonic Flow," Ph.D. thesis, Universidad Politécnica de Madrid, 2014.

[36] Canuto, C., Hussaini, M. Y., Quarteroni, A., and Zang, T. A., *Spectral methods in fluid dynamics*, Springer, 1987.

[37] Chang, C.-L., "Langley Stability and Transition Analysis Code (LASTRAC) Version 1.2 User Manual," NASA TM-2004-213233, 2004.

[38] Horstmann, K., Redeker, G., Quast, A., Dressler, U., and Bieler, H., "Flight Test Wih a Natural Laminar Flow Glove on a Transport Aircraft," AIAA 90-3044, 1990.

[39] Arnal, D., "Boundary Layer Transition: Prediction Based on Linear Theory," *Special course on Progress in Transition Modeling. AGARD. R-793*, 1994, pp. 1–62.

[40] Vassberg, J. C., DeHaan, M. A., Rivers, M. S., and Wahls, R. A., "Restrospective on the Common Research Model for Computational Fluid Dynamics Validation Studies," *Journal of Aircraft*, Vol. 55, No. 4, 2018, pp. 1325–1337. doi: 10.2514/1.C034906.

[41] Campbell, R. L., and Lynde, M., "Expanding the Natural Laminar Flow Boundary for Supersonic Transports," AIAA Paper 2016-4327, 2016. doi:10.2514/6.2016-4327.

[42] Lynde, M. N., and Campbell, R. L., "Computational Design and Analysis of a Transonic Natural Laminar Flow Wing for a Wind Tunnel Model," AIAA Paper 2017-3058, 2017. doi:10.2514/6.2017-3058.

[43] Crouch, J., Sutanto, M., Witkowski, D., Watkins, A., Rivers, M., and Campbell, R., "Assessment of the National Transition Facility for Natural Laminar Flow Testing," AIAA Paper 2010-1302, 2010. doi:10.2514/6.2010-1302.

[44] Mack, L., "Transition Prediction and Linear Stability Theory," *Laminar-Turbulent Transition. AGARD. CP-224*, 1977, pp. 1.1–1.22.

[45] King, R., Andino, M., Melton, L., Eppink, J., and Kegerise, M., "Flow Disturbance Measruements in the NationalTransonicFacility," *AIAA Journal*, Vol. 52, No. 1, 2014, pp. 116–130. doi:10.2514/1.J052429.

[46] Nichols, H., and Buning, P., "User's Manual for OVERFLOW 2.3," , August 2019. URL `https://overflow.larc.nasa.gov/home/users-manual-for-overflow-2-3/`.

[47] Spalart, P., and Allmaras, S., "A One-Equation Turbulence Model for Aerodynamc Flows," *Recherche Aerospatiale*, Vol. 1, 1994, pp. 5–21.

[48] Roe, P. L., "Approximate Riemann Solvers, Parameter Vectors, and Difference Schemes," *Journal of Computational Physics*, Vol. 43, No. 2, 1981, pp. 357–372.

[49] Nichols, R., Tramel, R., and Buning, P., "Solver and Turbulence Model Upgrades to OVERFLOW 2 for Unsteady and High-Speed Applications," AIAA Paper 2006-2824, 2006. doi:10.2514/6.2006-2824.